Three-Dimensional Terahertz Imaging Based on Piecewise Constant Doppler Algorithm and Step-Frequency Continuous-Wave Signalling

Yijiang Nan, Xiaojing Huang, *Senior Member, IEEE,* Xiang Gao, and Y. Jay Guo, *Fellow, IEEE*

Abstract—A novel 3-D time-domain Teraherz (THz) imaging system based on piecewise constant Doppler (PCD) algorithm and step-frequency continuous-wave (SFCW) signalling is proposed in this paper. Firstly, the SFCW THz imaging system configuration and the Gaussian beam propagation model are introduced. Then, the conventional time-domain correlation imaging algorithm is reviewed and the close-form expression of its point spread function (PSF) is derived to quantify the range and lateral resolutions. To reduce the computational complexity, a 2-D recursive imaging process based on the plane approximation of the range surface is proposed, by which the original PCD algorithm is extended for 3-D imaging with 2-D aperture synthesis. The 3-D PCD imaging principle, implementation and complexity analysis are discussed afterwards. Finally, simulation and experimental results are provided to validate the theoretical analysis of the 3-D time-domain THz imaging and demonstrate the high quality of the proposed imaging algorithm at low computational cost.

Index Terms—3-D imaging, Terahertz, step-frequency continuous-wave, Gaussian beam, time-domain correlation imaging, piecewise constant Doppler algorithm.

I. INTRODUCTION

TERAHERTZ (THz) imaging can offer many advantages due to its unique spectral characteristics: (1) THz wave can penetrate the obscuring materials such as clothes, plastics and packages; (2) THz wave is a non-ionizing radiation that does not have enough energy to remove an electron from an atom or molecule, thus is harmless to human beings and animals; (3) THz imaging can achieve a higher spatial resolution with small form factor compared with millimetre wave or low-frequency imaging due to the shorter THz signal wavelength. Consequently, THz imaging plays an important role in a wide variety of civil and public safety applications such as security inspection [1]–[3] at airports and railway stations, industrial nondestructive testing [4], [5], and medical personnel scanning [6], [7].

The reconstruction of a three-dimensional (3-D) THz image of objects to be observed is generally achieved by illuminating them with wideband THz wave and then recording and processing the scattered echoes with a two-dimensional (2-D) planar array [8]–[12]. The current state-of-the-art radio imaging techniques can be classified into two categories in terms of achieving 2-D spatial sampling. The first technique

Yijiang Nan, Xiaojing Huang and Y. Jay Guo are with Global Big Data Technologies Center, University of Technology Sydney, NSW, Australia. Xiang Gao is with School of Information and Electronics, Beijing Institute of Technology, Beijing, China. E-mails: yijiang.nan@uts.edu.au, xiaojing.huang@uts.edu.au, gaox@bit.edu.cn, and jay.guo@uts.edu.au.

uses the focal-plane array (FPA) [13], [14] that is placed behind a large lens and then focuses the image at the focal plane. However, the implementation of FPA in THz imaging system requires large and high cost array transceivers, and the spatial resolution at a far imaging distance is limited by the high optical $\mathbf{F}$-number, i.e., the ratio between focal length and antenna aperture. The second technique adopts the aperture synthesis by which a large 2-D aperture sampling can be accomplished with mechanical scanning of a monostatic transmit/receive (T/R) antenna or linear multi-static T/R antenna array [8], [15], [16]. The phase and amplitude of the coherently received data can be recorded, digitalized, and processed to reconstruct a high-resolution THz image without the lens, thus allowing focusing at any depth. Although a longer data acquisition time and more accurate antenna positioning are required for THz imaging, the use of aperture synthesis can improve the spatial resolution and simplify the array transceivers, which is more important for a practical THz imaging system.

The current 3-D microwave and THz imaging algorithms, e.g., range migration algorithm (RMA) [9]–[12], are generally derived from the exploding reflector model, by which the reconstructed image is actually the field of the echoes at the reflection point where the transmitter is located. Based on fast Fourier transform (FFT), the 3-D raw data can be processed in spatial frequency domains. After a phase migration operation along the transmission propagation direction, the image can be reconstructed after two-dimensional inverse FFT (IFFT). However, such FFT-based THz imaging algorithms have some intrinsic limitations due to the operation in spatial frequency domain. Firstly, the FFT operation requires a uniform spatial sampling in 2-D aperture, leading to an inflexible system configuration [8]. Secondly, the range cell migration (RCM) [9], [17] leads to the samples placed nonuniformly in spatial frequency domain [18]. This has to be compensated by using linear interpolation techniques. Thirdly, the size of the reconstructed image is quite small due to the short radius of the beam spot at the observed scene. Therefore, the FFT-based methods have to reconstruct several subimages block by block and then perform image stitching to form a large image. There are also many imaging algorithms based on time-domain correlation [18], [19] which process the received data directly in spatial domain and remove the intrinsic limitations of the FFT-based methods. However, the huge computational cost and data storage limit their practical applications. A novel time-domain imaging method, termed piecewise constant Doppler (PCD)

imaging [20]–[22], has been proposed recently for synthetic aperture radar (SAR) based on the linear approximation of the range curve, thus reducing the computational cost significantly. The original PCD algorithm reconstructs the image recursively along the radar trajectory for 2-D generalized continuous wave synthetic aperture radar (GCW-SAR) imaging. It cannot be used directly in the 3-D THz imaging due to the 2-D spatial sampling and the Gaussian beam propagation model [10], [23].

In this paper, a fully 3-D THz imaging system based on PCD principle and step-frequency continuous-wave (SFCW) signalling is developed. Instead of using the high cost and complicated THz array, a single-channel THz system with separate transmit and receive THz antennas is used to achieve the 2-D spatial sampling by illuminating the observed scene with a wideband SFCW signal. The system configuration is described, followed by the Gaussian beam propagation model. Based on the stop-and-go approximation and the back-projection (BP) algorithm, the 3-D time-domain correlation THz imaging process is presented. To benchmark the spatial resolutions and imaging performance of the time-domain THz imaging method, we derive the close-form expression of its point spread function (PSF) from which the lateral and range resolutions are shown to be determined by the equivalent beam waist and the transmitted bandwidth respectively. To reduce the huge computational cost of direct time-domain correlation, a 3-D PCD THz imaging algorithm is proposed based on the plane approximation of the range surface after extending the PCD principle to 2-D spatial sampling under Gaussian beam model. Analysis and simulation results demonstrate its superior performance over conventional time-domain correlation methods. An experimental monostatic THz imaging system with a 0.2-THz Gaussian beam transceiver is implemented to demonstrate its practical application.

The reminder of this paper is organized as follows. In Section II, the system configuration and the THz propagation model are firstly presented and then the close-form expression of the PSF is derived. The proposed 3-D PCD THz imaging algorithm is proposed in Section III with the imaging implementation and the complexity analysis. Simulation and experimental results are shown in Section IV and V respectively to validate the theoretical analysis of time-domain correlation imaging and the practical performance of the proposed PCD method. Finally, conclusions are drawn in Section VI.

II. 3-D TIME-DOMAIN CORRELATION THz IMAGING

In this section, we first introduce the system configuration of the monostatic THz imaging and the Gaussian beam propagation model with the SFCW transmitted waveform. We then describe the 3-D time-domain correlation THz imaging method and derive the close-form expression of its PSF accordingly.

A. System Configuration

The block diagram of the single-channel 3-D THz imaging scheme based on SFCW signalling is illustrated in Fig. 1. A relatively low-frequency SFCW signal is generated and upconverted with a multiplier to THz band. The radiation beam
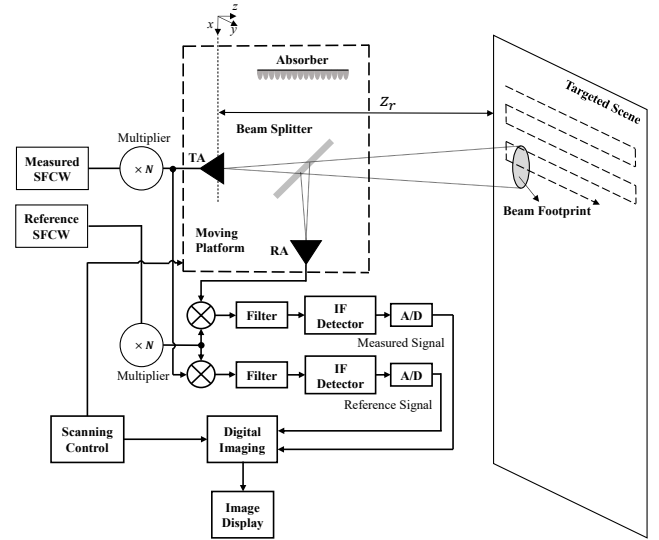

Fig. 1. Single-channel 3-D THz imaging scheme based on SFCW signal.

is transmitted by a THz antenna and the scattered echoes are received by a separate THz receive antenna through a beam splitter. The unwanted transmitted and received THz waves are removed by a THz absorber. Another SFCW generator provides a local oscillator (LO) SFCW signal which is also upconverted to THz band and mixed with the transmitted and received signals to produce the measured and reference signals respectively. After analog-to-digital conversion (A/D), the coherent measured and reference signals are processed to focus the targeted image. To achieve a 2-D spatial sampling, the transmit and receive antennas (TA and RA), the beam splitter and absorber are installed on a quasi-optics moving platform which is driven by a scanning controller. The transmit antenna, at a distance z_r, scans the targeted area laterally in x- and y-directions at a constant speed and its location information is also transferred to the digital imaging module.

B. THz Propagation Model and Scattered Echoes

Working in an extreme high-frequency band, the transmitted beam in a THz system is always generated based on a series of quasi-optics equipment, thus following the Gaussian beam propagation model which is derived by solving the Maxwell equations in paraxial approximation [23]. Assuming that the transmitted THz Gaussian beam propagates in $+z$-direction, the phase center is located at $(x, y, 0)$ and the beam waist radius is equal to ω_0 at the plane $z = 0$, the transmitted field at the target located at (x', y', z') can be described as

$$
\begin{aligned}
&E_t(x', y', z'; x, y, k) \\
&= \frac{A_0}{W(z', k)} \cdot exp(-\frac{\rho^2(x', y'; x, y)}{W^2(z', k)}) \\
&\quad \cdot exp(-jk(z' + \frac{\rho^2(x', y'; x, y)}{2R(z', k)}) + j\phi(z', k))
\end{aligned}
\tag{1}
$$

where A_0 is the amplitude of the beam center, $\rho^2(x', y'; x, y) = (x - x')^2 + (y - y')^2$, $W(z', k)$, $R(z', k)$ and $\phi(z', k)$ are the beam footprint radius, the wavefront

radius and the initial phase at the plane $z = z'$ respectively, expressed as

$$W(z', k) = \omega_0 \sqrt{1 + (\frac{2z'}{k\omega_0^2})^2}, \qquad (2)$$

$$R(z', k) = z'(1 + (\frac{k\omega_0^2}{2z'})^2) \qquad (3)$$

and

$$\phi(z', k) = arctg(\frac{2z'}{k\omega_0^2}) \qquad (4)$$

where $k = 2\pi f/c$ is the wavenumber corresponding to the temporal frequency f in the transmitted SFCW signal and c is the light speed.

The received signal is actually a superposition of the echoes from the targeted domain D. Due to the round trip propagation, the scattered field can be derived as

$$
\begin{aligned}
& E_r(x, y, k) \\
& = \iiint_D \sigma(x', y', z') E_t^2(x', y', z'; x, y, k) dx' dy' dz' \\
& \approx \iiint_D \sigma(x', y', z') \frac{A_0^2}{W^2(z', k)} \\
& \cdot exp(-\frac{2\rho^2(x', y'; x, y)}{W^2(z', k)}) \\
& \cdot exp(-j2k(z' + \frac{\rho^2(x', y'; x, y)}{2R(z', k)})) dx' dy' dz'
\end{aligned}
\qquad (5)
$$

where the phase term $\phi(z', k)$ can be neglected in the imaging process since the range of its variation is much smaller than that of $k(z' + \frac{\rho^2(x', y'; x, y)}{2R(z', k)})$ due to $z' \gg f_c/c$ [10].

C. Imaging Process

The conventional 3-D time-domain correlation imaging algorithm is presented in this subsection. Following the stop-and-go approximation and slow time 2-D sampling, the image can be reconstructed by the range compression and the BP algorithm respectively. To derive the PSF of the time-domain THz imaging, we only consider a one-point target located at $(0, 0, z_r)$ and the scattered field can be expressed as

$$
\begin{aligned}
& E_r(x, y, k) \\
& = \sigma(0, 0, z_r) \frac{A_0^2}{W^2(z_r, k)} \cdot exp(-\frac{2\rho^2(0, 0; x, y)}{W^2(z_r, k)}) \\
& \cdot exp(-j2k(z_r + \frac{\rho^2(0, 0; x, y)}{2R(z_r, k)})).
\end{aligned}
\qquad (6)
$$

With a narrow-bandwidth SFCW signal, we have $W(z_r, k) \approx W(z_r, k_c)$ and $R(z_r, k) \approx R(z_r, k_c)$ where $k \approx k_c = 2\pi f_c/c$ and f_c is the transmitted signal centre frequency. The range compressed image can be achieved after the IFFT operation with respect to the wavenumber k as

$$
\begin{aligned}
& e_r(x, y, z'') \\
& = \int_{\frac{2\pi f_c - \pi B}{c}}^{\frac{2\pi f_c + \pi B}{c}} E_r(x, y, k) exp(j2kz'') dk \\
& = \int_{-\frac{\pi B}{c}}^{\frac{\pi B}{c}} \sigma(0, 0, z_r) \frac{A_0^2}{W^2(z_r, k_c)} \cdot exp(-\frac{2\rho^2(0, 0; x, y)}{W^2(z_r, k_c)}) \\
& \cdot exp(-j2k(z_r + \frac{\rho^2(0, 0; x, y)}{2R(z_r, k_c)})) \\
& \cdot exp(-j\frac{4\pi}{\lambda_c}(z_r + \frac{\rho^2(0, 0; x, y)}{2R(z_r, k_c)})) exp(j2kz'') dk \\
& \approx \sigma(0, 0, z_r) \frac{A_0^2}{W^2(z_r, k_c)} \cdot exp(-\frac{2\rho^2(0, 0; x, y)}{W^2(z_r, k_c)}) \\
& \cdot sinc(\frac{2\pi B}{c}(z'' - (z_r + \frac{\rho^2(0, 0; x, y)}{2R(z_r, k_c)}))) \\
& \cdot exp(-j\frac{4\pi}{\lambda_c}(z_r + \frac{\rho^2(0, 0; x, y)}{2R(z_r, k_c)}))
\end{aligned}
\qquad (7)
$$

where $\lambda_c = c/f_c$ and B are the wavelength and the bandwidth of the transmitted SFCW signal respectively and the sinc function is defined as $sinc(x) = sin(x)/x$. We can see that the image in range has been compressed but RCM compensation is required in lateral imaging process. To do so, we multiply (7) by a Dirac Delta function $\delta(z'' - (z' + \frac{\rho^2(x', y'; x, y)}{2R(z', k_c)}))$ and then reconstruct the image based on the BP algorithm as

$$
\begin{aligned}
& I(x', y', z') \\
& = \iint e_r(x, y, z'') \delta(z'' - (z' + \frac{\rho^2(x', y'; x, y)}{2R(z', k_c)})) \\
& \cdot exp(j\frac{4\pi}{\lambda_c}(z' + \frac{\rho^2(x', y'; x, y)}{2R(z', k_c)})) dx dy \\
& = \iint \sigma(0, 0, z_r) \frac{A_0^2}{W^2(z_r, k_c)} \cdot exp(-\frac{2\rho^2(0, 0; x, y)}{W^2(z_r, k_c)}) \\
& \cdot sinc(\frac{2\pi B}{c}((z' + \frac{\rho^2(x', y'; x, y)}{2R(z', k_c)}) - (z_r + \frac{\rho^2(0, 0; x, y)}{2R(z_r, k_c)}))) \\
& \cdot exp(j\frac{4\pi}{\lambda_c}(z' - z_r + \frac{\rho^2(x', y'; x, y)}{2R(z', k_c)} - \frac{\rho^2(0, 0; x, y)}{2R(z_r, k_c)})) dx dy
\end{aligned}
\qquad (8)
$$

which is the PSF of the 3-D time-domain THz imaging. To derive the range and lateral resolutions, two cases, i.e., $I(0, 0, z')$ and $I(x', y', z_r)$, are considered respectively. Note that the 3-dB energy cut-off point of the PSF is defined as the resolution.

1) Range Resolution: When $x' = 0$ and $y' = 0$, the range image can be reconstructed as

$$
\begin{aligned}
&I(0,0,z') \\
&\approx \sigma(0,0,z_r)\frac{A_0^2}{W^2(z_r,k_c)} \cdot sinc(\frac{2\pi B}{c}(z'-z_r)) \\
&\cdot exp(j\frac{4\pi}{\lambda_c}(z'-z_r)) \int\int exp(-\frac{2\rho^2(0,0;x,y)}{W^2(z_r,k_c)})dxdy \\
&= \sigma(0,0,z_r)\frac{A_0^2}{W^2(z_r,k_c)} \cdot sinc(\frac{2\pi B}{c}(z'-z_r)) \\
&\cdot exp(j\frac{4\pi}{\lambda_c}(z'-z_r)) \cdot \pi \int exp(-\frac{2\rho_r^2}{W^2(z_r,k_c)})d\rho_r^2 \\
&= \sigma(0,0,z_r)\pi\frac{A_0^2}{2}sinc(\frac{2\pi B}{c}(z'-z_r))exp(j\frac{4\pi}{\lambda_c}(z'-z_r))
\end{aligned}
\tag{9}
$$

where $\frac{\rho^2(0,0;x,y)}{2R(z',k_c)} - \frac{\rho^2(0,0;x,y)}{2R(z_r,k_c)} \approx 0$ is assumed since $R(z) \gg W(z)$ in a far-field THz imaging system and the integral over x-y plane is replaced by that over radius $\rho_r = \rho(0,0;x,y)$. Hence, the range resolution δ_z is determined at the 3-dB energy cut-off point $2\pi B(z'-z_r)/c \approx 0.88\pi$ when $z'-z_r = \delta_z$ and expressed as

$$
\delta_z = 0.44\frac{c}{B}
\tag{10}
$$

which is only determined by the transmitted bandwidth.

2) Lateral Resolution: When $z' = z_r$, from (8), the lateral image can be reconstructed as

$$
\begin{aligned}
&I(x',y',z_r) \\
&\approx \int\int \sigma(0,0,z_r)\frac{A_0^2}{W^2(z_r,k_c)} \cdot exp(-\frac{2\rho^2(0,0;x,y)}{W^2(z_r,k_c)}) \\
&\cdot exp(j\frac{2\pi}{\lambda_c R(z_r,k_c)}(\rho^2(x',y';x,y)-\rho^2(0,0;x,y)))dxdy \\
&= \sigma(0,0,z_r)\frac{A_0^2}{W^2(z_r,k_c)}exp(j\frac{2\pi x'^2}{\lambda_c R(z_r,k_c)})exp(j\frac{2\pi y'^2}{\lambda_c R(z_r,k_c)}) \\
&\cdot \int exp(-\frac{2x^2}{W^2(z_r,k_c)})exp(-j\frac{4\pi x'x}{\lambda_c R(z_r,k_c)})dx \\
&\cdot \int exp(-\frac{2y^2}{W^2(z_r,k_c)})exp(-j\frac{4\pi y'y}{\lambda_c R(z_r,k_c)})dy
\end{aligned}
\tag{11}
$$

where $\frac{\rho^2(x',y';x,y)}{2R(z_r,k_c)} - \frac{\rho^2(0,0;x,y)}{2R(z_r,k_c)} \approx 0$ is assumed in the sinc function since $R(z) \gg W(z)$. We can see from (11) that the two integral can be considered as the Fourier transform of $exp(-\frac{2x^2}{W^2(z_r)})$ and $exp(-\frac{2y^2}{W^2(z_r)})$ with respect to x and y respectively. Substituting $\sqrt{\pi}exp(-\frac{x'^2}{4}) = \int exp(-x^2) \cdot$

$exp(-jx'x)dx$ into (11), $I(x',y',z_r)$ can be derived as

$$
\begin{aligned}
&I(x',y',z_r) \\
&= \sigma(0,0,z_r)\frac{A_0^2}{W^2(z_r,k_c)}exp(j\frac{2\pi x'^2}{\lambda_c R(z_r,k_c)}) \\
&\cdot exp(j\frac{2\pi y'^2}{\lambda_c R(z_r,k_c)})\frac{W(z_r,k_c)}{\sqrt{2}} \\
&\cdot \int exp(-x^2)exp(-j\frac{4\pi W(z_r,k_c)x'x}{\sqrt{2}\lambda_c R(z_r,k_c)})dx \\
&\cdot \frac{W(z_r,k_c)}{\sqrt{2}} \int exp(-y^2)exp(-j\frac{4\pi W(z_r,k_c)y'y}{\sqrt{2}\lambda_c R(z_r,k_c)})dy \\
&= \sigma(0,0,z_r)\frac{A_0^2}{2}exp(j\frac{2\pi(x'^2+y'^2)}{\lambda_c R(z_r,k_c)}) \\
&\cdot \int exp(-x^2)exp(-j\frac{\sqrt{2}k_c W(z_r,k_c)x'x}{R(z_r,k_c)})dx \\
&\cdot \int exp(-y^2)exp(-j\frac{\sqrt{2}k_c W(z_r,k_c)y'y}{R(z_r,k_c)})dy \\
&= \sigma(0,0,z_r)\pi\frac{A_0^2}{2}exp(j\frac{2\pi(x'^2+y'^2)}{\lambda_c R(z_r,k_c)}) \\
&\cdot exp(-\frac{k_c^2 W^2(z_r,k_c)}{2R^2(z_r,k_c)}(x'^2+y'^2)).
\end{aligned}
\tag{12}
$$

Based on (2) and (3), (12) can be further derived as

$$
\begin{aligned}
&I(x',y',z_r) \\
&= \sigma(0,0,z_r)\pi\frac{A_0^2}{2}exp(j\frac{2\pi(x'^2+y'^2)}{\lambda_c R(z_r,k_c)}) \\
&\cdot exp(-\frac{8z_r^2}{k_c^2 w_0^4 + 4z_r^2} \cdot \frac{x'^2+y'^2}{w_0^2}) \\
&\approx \sigma(0,0,z_r)\pi\frac{A_0^2}{2}exp(-\frac{2(x'^2+y'^2)}{w_0^2})exp(j\frac{2\pi(x'^2+y'^2)}{\lambda_c R(z_r,k_c)})
\end{aligned}
\tag{13}
$$

where $2z_r \gg k_c w_0^2$ is assumed in a far-field THz imaging system. The lateral resolution δ_l can be derived based on the 3-dB energy cut-off point of (13), i.e., $-2(x'^2+y'^2)/w_0^2 \approx -1.3778$, when $x'^2+y'^2 = \delta_l^2$, as

$$
\delta_l = 0.83w_0
\tag{14}
$$

which is only determined by the equivalent beam waist.

III. 3-D PCD THz IMAGING

With the conventional 3-D time-domain THz imaging method described in Section II.C, every image pixel has to be reconstructed independently by a correlation over a 2-D synthetic aperture, thus leading to a huge computational cost. In this section, a novel fast 3-D time-domain THz imaging is proposed based on the PCD principle by which the correlation is calculated recursively after the plane approximation to the range surface.

A. Recursive Imaging Principle

In 3-D THz imaging, the spatial received samples are acquired by using a 2-D aperture synthesis. Based on Gaussian beam propagation, the instantaneous range between the receive
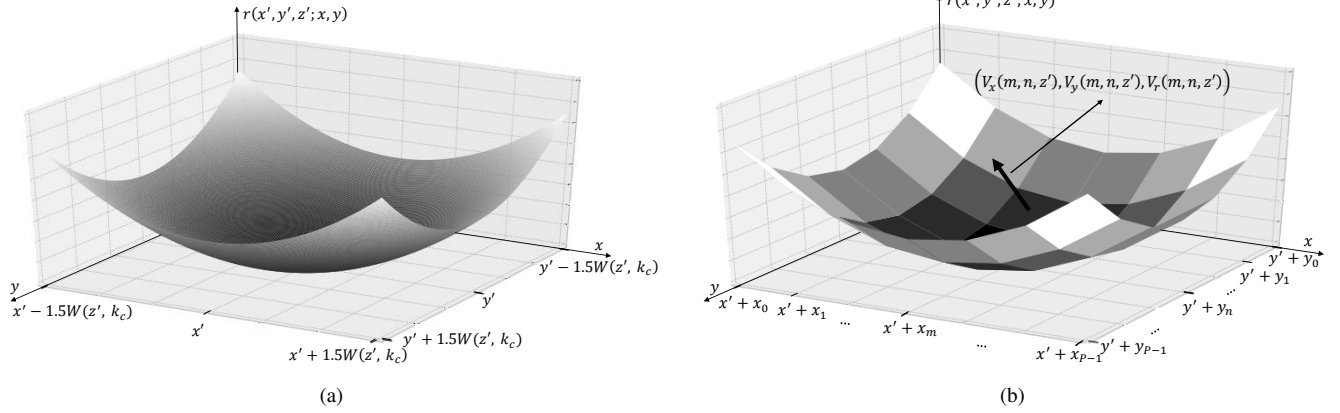
Fig. 2. Range surface in 3-D THz imaging: (a) original range surface $r(x', y', z'; x, y)$ and (b) plane approximated range surface $\tilde{r}(x', y', z'; x, y)$.
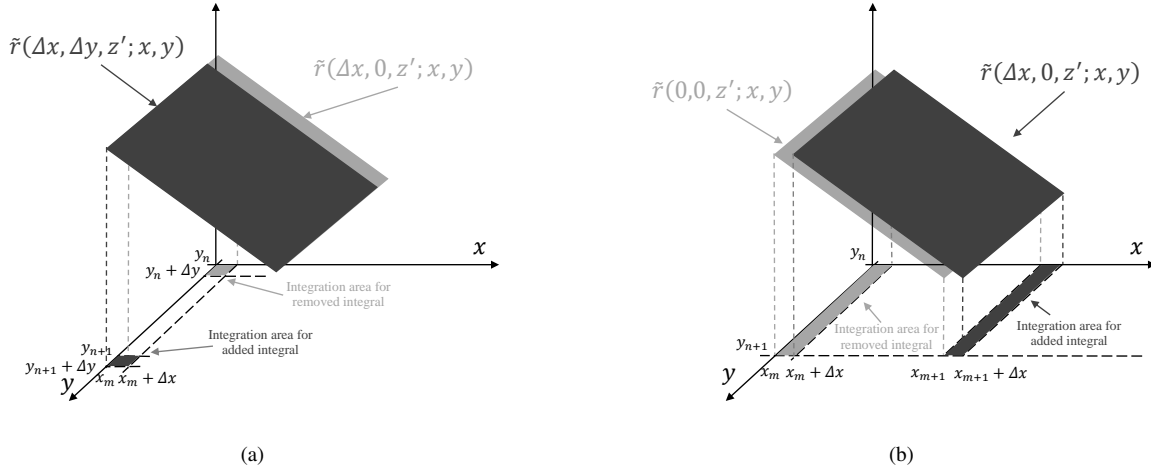

Fig. 3. 2-D recursive imaging process: (a) $S_{m,n}(x' + \delta x, y' + \delta y, z')$ update and (b) $I_{m,n}(x' + \delta x, y', z')$ update.

antenna and the target located at (x', y', z') can be expressed as $r(x', y', z'; x, y) = z' + \frac{\rho^2(x', y'; x, y)}{2R(z', k_c)}$, thus forming a parabolic surface shown in Fig. 2a.

Given the radius of the beam footprint $W(z', k_c)$ at the plane $z = z'$, to reconstruct the image, the integration area is defined by the intervals in x- and y-directions set from $x' - 1.5 \cdot W(z', k_c)$ to $x' + 1.5 \cdot W(z', k_c)$ and from $y' - 1.5 \cdot W(z', k_c)$ to $y' + 1.5 \cdot W(z', k_c)$ respectively to capture almost all the energy of the beam. Similar to the piecewise linear approximation of the range curve in GCW-SAR imaging [22], the surface represented by $r(x', y', z'; x, y)$ can be approximated as $P \times P$ planes represented by $\tilde{r}(x', y', z'; x, y)$, which is termed as plane approximation shown in Fig. 2b. The integration areas over the respective $P \times P$ planes are obtained by dividing the dimensions of the original integration area in x and y axises into P segments with the segment joint points at $x_m = -1.5 \cdot W(z', k_c) + \frac{3W(z', k_c)}{P} \cdot m$ and $y_n = -1.5 \cdot W(z', k_c) + \frac{3W(z', k_c)}{P} \cdot n$ for $m = 0, 1, 2, ..., P-1$ and $n = 0, 1, 2, ..., P-1$ respectively. Therefore, the reconstructed image $I(x', y', z')$ can be computed as a sum of integrals over $P \times P$ individual

planes after range compression, i.e.,

$$I(x', y', z') = \sum_{m=0}^{P-1} \sum_{n=0}^{P-1} I_{m,n}(x', y', z'). \tag{15}$$

The integral $I_{m,n}(x', y', z')$ over the plane at (x_m, y_n) can be obtained as

$$
\begin{aligned}
& I_{m,n}(x', y', z') \\
&= \int_{x'+x_m}^{x'+x_{m+1}} \int_{y'+y_n}^{y'+y_{n+1}} e_r(x, y, \tilde{r}(x', y', z'; x, y)) \\
& \cdot exp(j \frac{4\pi}{\lambda_c} \tilde{r}(x', y', z'; x, y)) dy dx
\end{aligned}
\tag{16}
$$

where the approximated range $\tilde{r}(x', y', z'; x, y)$ is determined by the three points $(x' + x_m, y' + y_n, r(x', y', z'; x' + x_m, y' + y_n))$, $(x' + x_{m+1}, y' + y_n, r(x', y', z'; x' + x_{m+1}, y' + y_n))$, and $(x' + x_m, y' + y_{n+1}, r(x', y', z'; x' + x_m, y' + y_{n+1}))$ on the original range surface. Based on these three points, the plane's normal vector $(V_x(m, n, z'), V_y(m, n, z'), V_r(m, n, z'))$ can be derived as shown in (17) at top of next page, where $\vec{i}$, $\vec{j}$, and $\vec{k}$ represent the unit vectors in x-, y- and r-directions

$$
\begin{aligned}
&(V_x(m,n,z'), V_y(m,n,z'), V_r(m,n,z')) \\
&= \begin{vmatrix}
\vec{i} & \vec{j} & \vec{k} \\
x_m - x_{m+1} & 0 & r(x',y',z';x'+x_m, y'+y_n) - r(x',y',z';x'+x_{m+1}, y'+y_n) \\
0 & y_n - y_{n+1} & r(x',y',z';x'+x_m, y'+y_n) - r(x',y',z';x'+x_m, y'+y_{n+1})
\end{vmatrix} \\
&= \Big((y_{n+1} - y_n) \cdot (r(0,0,z';x_m,y_n) - r(0,0,z';x_{m+1},y_n)), (x_{m+1} - x_m) \cdot (r(0,0,z';x_m,y_n) \\
&\quad - r(0,0,z';x_m,y_{n+1})), (x_m - x_{m+1})(y_n - y_{n+1}) \Big)
\end{aligned}
\tag{17}
$$

respectively. With the normal vector, the approximated range on the plane at (x_m, y_n) can be expressed as

$$
\begin{aligned}
\tilde{r}(x',y',z';x,y) &= \frac{V_x(m,n,z')}{V_r(m,n,z')}(x'+x_m - x) \\
&\quad + \frac{V_y(m,n,z')}{V_r(m,n,z')}(y'+y_n - y) \\
&\quad + r(x',y',z';x'+x_m, y'+y_n) \\
&= D_x(m,n,z')(x'+x_m - x) \\
&\quad + D_y(m,n,z')(y'+y_n - y) \\
&\quad + r(0,0,z';x_m,y_n)
\end{aligned}
\tag{18}
$$

which has linear variations in x- and y-directions respectively, i.e., the slopes in x- and y-directions, denoted as $D_x(m,n,z') = V_x(m,n,z')/V_r(m,n,z')$ and $D_y(m,n,z') = V_y(m,n,z')/V_r(m,n,z')$, are constant for the plane at (x_m, y_n).

Making use of the constant slopes for each plane on the approximated range surface, a recursive imaging process can be derived similar to the original PCD algorithm. Hence, given the imaging spacing Δx in the x-direction, $I_{m,n}(x' + \Delta x, y', z')$ can be calculated recursively along x-direction from $I_{m,n}(x', y', z')$ as

$$
\begin{aligned}
&I_{m,n}(x' + \Delta x, y', z') \\
&\approx \int_{x'+\Delta x+x_m}^{x'+\Delta x+x_{m+1}} \int_{y'+y_n}^{y'+y_{n+1}} e_r(x,y,\tilde{r}(x',y',z';x,y)) \\
&\quad \cdot exp(j\frac{4\pi}{\lambda_c}(D_x(m,n,z')(x'+\Delta x+x_m - x) \\
&\quad + D_y(m,n,z')(y'+y_n - y) + r(0,0,z';x_m,y_n)))dydx \\
&= I_{m,n}(x',y',z') \cdot exp(j\frac{4\pi}{\lambda_c}D_x(m,n,z')\Delta x) \\
&\quad - \int_{x_m}^{\Delta x+x_m} \int_{y_n}^{y_{n+1}} e_r(x'+x, y'+y, \tilde{r}(\Delta x, 0, z';x,y)) \\
&\quad \cdot exp(j\frac{4\pi}{\lambda_c}\tilde{r}(\Delta x, 0, z';x,y))dydx \\
&\quad + \int_{x_{m+1}}^{\Delta x+x_{m+1}} \int_{y_n}^{y_{n+1}} e_r(x'+x, y'+y, \tilde{r}(\Delta x, 0, z';x,y)) \\
&\quad \cdot exp(j\frac{4\pi}{\lambda_c}\tilde{r}(\Delta x, 0, z';x,y))dydx
\end{aligned}
\tag{19}
$$

where $\tilde{r}(x'+\Delta x, y', z'; x'+x, y'+y) = \tilde{r}(\Delta x, 0, z';x,y)$, and $e_r(x,y,\tilde{r}(x'+\Delta x, y', z';x,y)) \approx e_r(x,y,\tilde{r}(x',y',z';x,y))$ is valid due to the short interval $(x_m, x_{m+1}]$ and $(y_n, y_{n+1}]$.

Compared with the original PCD imaging, an extra independent spatial correlation represented by the integral over the interval $(y_n, y_{n+1}]$ in y-direction as shown in (19) is necessary before the recursive imaging in x-direction. To further reduce the computational cost, the integral over the area enclosed by x interval $(x_m, \Delta x + x_m]$ and y interval $(y_n, y_{n+1}]$ in (19) defined as

$$
\begin{aligned}
&S_{m,n}(x' + \Delta x, y', z') \\
&= \int_{x_m}^{\Delta x+x_m} \int_{y_n}^{y_{n+1}} e_r(x'+x, y'+y, \tilde{r}(\Delta x, 0, z';x,y)) \\
&\quad \cdot exp(j\frac{4\pi}{\lambda_c}\tilde{r}(\Delta x, 0, z';x,y))dydx
\end{aligned}
\tag{20}
$$

can be also calculated recursively along y-direction. Since $e_r(x,y,\tilde{r}(x'+\Delta x, y'+\Delta y, z';x,y)) \approx e_r(x,y,\tilde{r}(x'+\Delta x, y', z';x,y))$ is valid when $x \in (x_m, x_{m+1}]$ and $y \in (y_n, y_{n+1}]$, $S_{m,n}(x'+\Delta x, y'+\Delta y, z')$ can be recursively calculated from $S_{m,n}(x'+\Delta x, y', z')$ as

$$
\begin{aligned}
&S_{m,n}(x' + \Delta x, y' + \Delta y, z') \\
&\approx \int_{x_m}^{\Delta x+x_m} \int_{\Delta y+y_n}^{\Delta y+y_{n+1}} e_r(x'+x, y'+y, \tilde{r}(\Delta x, 0, z';x,y)) \\
&\quad \cdot exp(j\frac{4\pi}{\lambda}(D_x(m,n,z')(\Delta x+x_m - x) \\
&\quad + D_y(m,n,z')(\Delta y+y_n - y) + r(0,0,z';x_m,y_n)))dydx \\
&= S_{m,n}(x'+\Delta x, y', z') \cdot exp(j\frac{4\pi}{\lambda_c}D_y(m,n,z')\Delta y) \\
&\quad - \int_{x_m}^{\Delta x+x_m} \int_{y_n}^{\Delta y+y_n} e_r(x'+x, y'+y, \tilde{r}(\Delta x, \Delta y, z';x,y)) \\
&\quad \cdot exp(j\frac{4\pi}{\lambda_c}\tilde{r}(\Delta x, \Delta y, z';x,y))dydx \\
&\quad + \int_{x_m}^{\Delta x+x_m} \int_{y_{n+1}}^{\Delta y+y_{n+1}} e_r(x'+x, y'+y, \tilde{r}(\Delta x, \Delta y, z';x,y)) \\
&\quad \cdot exp(j\frac{4\pi}{\lambda_c}\tilde{r}(\Delta x, \Delta y, z';x,y))dydx
\end{aligned}
\tag{21}
$$

where Δy is the imaging spacing in y-direction. The recursive process to calculate the integrals $S_{m,n}(x'+\Delta x, y'+\Delta y, z')$ and $I_{m,n}(x'+\Delta x, y, z')$ are shown in Fig. 3 respectively, where the integration areas for the integrals to be removed and added in (19) and (21) are indicated in grey and black colors respectively. The updated integral in x- or y-directions is obtained recursively by compensating the corresponding constant slope in the previous integral, removing an integral

over an imaging spacing in current plane, and adding an integral over an imaging spacing in next plane.

In summary, the above described recursive imaging method consists of four steps as follows.

1) Perform range compression achieved by IFFT operation to obtain $e_r(x, y, z'')$;
2) As the THz transmit antenna moves along y-direction, recursively update $S_{m,n}(x', y', z')$ for a given z' and all m and n;
3) Once a scanning in y-direction is completed and before next scanning in y-direction, recursively update $I_{m,n}(x', y', z')$ for a given z' and all m and n;
4) Sum up all $I_{m,n}(x', y', z')$ to reconstruct the image $I(x', y', z')$.

Repeat the above processes for different z', a 3-D image can be reconstructed. We call this recursive imaging method as 3-D PCD imaging. Though there is no explicit Doppler frequency involved, the principle of using plane approximation to obtain constant slopes of the discrete pieces on the range surface is similar to that of the original PCD imaging in GCW-SARs.

B. Recursive Imaging Implementation

Given a z', the proposed 2-D recursive imaging method in digital domain is presented in this subsection. For simplicity, the spatial sampling intervals in x- and y-directions are set equal to the imaging spacing Δx and Δy respectively. The recursive process in y-direction shown in (21) can be implemented as

$$
\begin{aligned}
&S_{m,n}(x' + \Delta x, y' + \Delta y, z') \\
&= S_{m,n}(x' + \Delta x, y', z') \cdot exp(j\frac{4\pi}{\lambda_c} D_y(m, n, z')\Delta y) \\
&- \Delta x \Delta y \cdot e_r(x' + \Delta x + x_m, y' + \Delta y + y_n, \\
&\tilde{r}(\Delta x, \Delta y, z'; \Delta x + x_m, \Delta y + y_n)) \\
&\cdot exp(j\frac{4\pi}{\lambda_c}\tilde{r}(\Delta x, \Delta y, z'; \Delta x + x_m, \Delta y + y_n)) \\
&+ \Delta x \Delta y \cdot e_r(x' + \Delta x + x_m, y' + \Delta y + y_{n+1}, \\
&\tilde{r}(\Delta x, \Delta y, z'; \Delta x + x_m, \Delta y + y_{n+1})) \\
&\cdot exp(j\frac{4\pi}{\lambda_c}\tilde{r}(\Delta x, \Delta y, z'; \Delta x + x_m, \Delta y + y_{n+1})) \\
&= S_{m,n}(x' + \Delta x, y', z') \cdot exp(j\frac{4\pi}{\lambda_c} D_y(m, n, z')\Delta y) \\
&- \Delta x \Delta y \cdot e_r(x' + \Delta x + x_m, y' + \Delta y + y_n, \\
&\tilde{r}(0, 0, z'; x_m, y_n)) \cdot exp(j\frac{4\pi}{\lambda_c}\tilde{r}(0, 0, z'; x_m, y_n)) \\
&+ \Delta x \Delta y \cdot e_r(x' + \Delta x + x_m, y' + \Delta y + y_{n+1}, \\
&\tilde{r}(0, 0, z'; x_m, y_{n+1})) \cdot exp(j\frac{4\pi}{\lambda_c}\tilde{r}(0, 0, z'; x_m, y_{n+1}))
\end{aligned}
\tag{22}
$$

and the recursive process in x-direction shown in (19) can be implemented as

$$
\begin{aligned}
&I_{m,n}(x' + \Delta x, y', z') \\
&= I_{m,n}(x', y', z') \cdot exp(j\frac{4\pi}{\lambda_c} D_x(m, n, z')\Delta x) \\
&- S_{m,n}(x' + \Delta x, y', z') + S_{m+1,n}(x' + \Delta x, y', z').
\end{aligned}
\tag{23}
$$

Taking $P = 4$ as an example, the 3-D PCD THz imaging implementation is illustrated in Fig. 4, where the steps of the 2-D recursive imaging for a given z' are illustrated in Fig. 4a, and the flow graphs of $S_{m,n}(x', y', z')$ update and $I_{m,n}(x', y', z')$ update are given in Fig. 4b and Fig. 4c respectively. It is shown that the 2-D recursive imaging method can be considered as two recursive processes in y- and x-directions respectively and the images in z-direction can be reconstructed in parallel at the same time.

C. Complexity

For the sake of complexity comparison, suppose that $N \times N \times N$ samples are recorded with one shot of the observed scene and an $N \times N \times N$ 3-D image is reconstructed by the direct time-domain correlation imaging algorithm and the proposed 3-D PCD imaging algorithm, respectively.

The direct time-domain correlation imaging algorithm reconstructs each image point individually from the range compressed data. To achieve an $N \times N \times N$ imaging, the total number of complex multiplication is $N^3 \log_2 N + N^4$. The 3-D PCD imaging algorithm updates the correlation recursively based on the plane approximation of the range surface. As shown in Fig. 4, the reconstruction of one image point requires $P+1$ recursive processes in step 2 and P recursive processes in step 3, and their corresponding required numbers of complex multiplications are $2P + 1$ and P respectively. Including the N^2 IFFT operations, the total number of complex multiplications is equal to $N^3 \log_2 N + N^2(3P^2 + 3P + 1)$. In a practical imaging system, P is always set much smaller than N, i.e., P^2 is approximately equal to N, and thus the complexity of the proposed PCD and time correlation imaging algorithms are $\mathcal{O}(N^3 \log_2 N)$ and $\mathcal{O}(N^4)$ respectively. Additionally, the PCD method can be achieved in parallel, which is well suited for field programmable gate array (FPGA) or graphics processing unit (GPU) based implementation, and hence the imaging time can be further reduced.

IV. SIMULATION RESULTS

In this section, simulation results based on the novel 3-D time-domain THz imaging with Gaussian propagation model are presented. To evaluate and compare the performance of 3-D time-domain correlation and 3-D PCD methods, the THz imaging systems operate under the same system configuration presented in Section II.A with the following parameters: equivalent beam waist 4.7mm, distance between transmitter and observed scene $z_r = 0.48$m, transmitted bandwidth is 19.2GHz, center frequency $f_c = 199.5$GHz, the number of frequency sweeping points $N_f = 201$, and the sampling intervals in x-directions and y-directions $\Delta x = 2$mm and $\Delta y = 2$mm respectively.

A. Time-Domain Correlation Imaging Performance for Point Target

To validate the theoretical analysis of the 3-D time-domain THz imaging, the performance of an ideal point target reconstructed by time-domain correlation imaging method is investigated in the first simulation experiment. The point target is
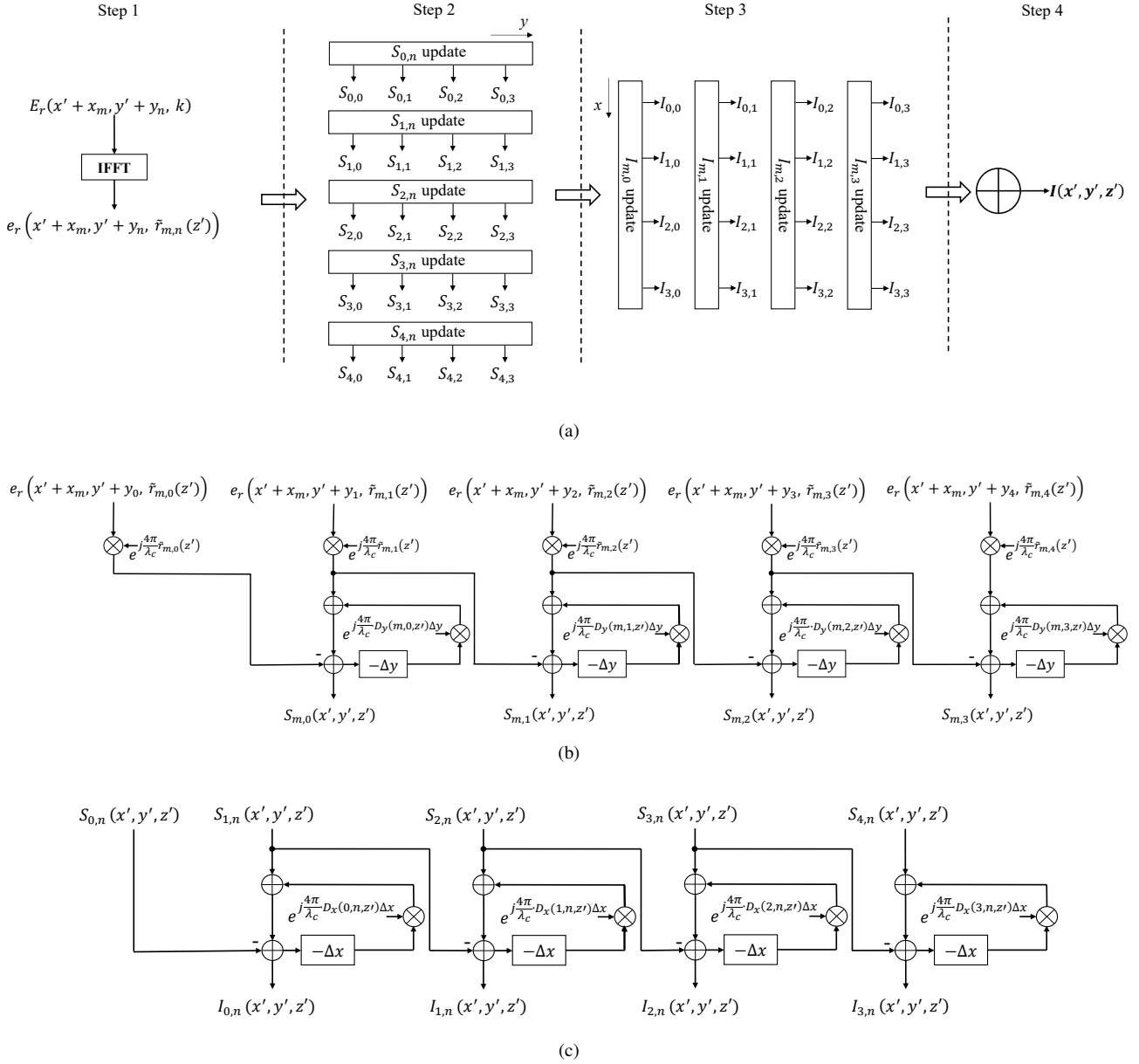
Fig. 4. 3-D PCD Thz imaging implementation for a given z', where $-\Delta y$ and $-\Delta x$ denote the spatial delays in y- and x-directions respectively, $S_{m,n}$ and $I_{m,n}$ denote $S_{m,n}(x',y',z')$ and $I_{m,n}(x',y',z')$ respectively, and $\widetilde{r}_{m,n}(z')$ denotes $\widetilde{r}(0,0,z';x_m,y_n)$: (a) steps of 2-D recursive imaging, (b) flow graph of $S_{m,n}(x',y',z')$ update, and (c) flow graph of $I_{m,n}(x',y',z')$ update.

located at $(0,0,0.48)$ and the size of synthetic aperture is set as $3W(z',k_c) \times 3W(z',k_c)$. The point-target image reconstructed by the time-domain correlation method is presented in Fig. 5. For comparison, the close-form expression of the PSF in range and lateral directions based on (9) and (13) are plotted in Fig. 5 respectively. The simulation results show that the PSF in range and lateral directions can be approximated as sinc and Gaussian functions respectively, validating the theoretical equations of the range and lateral resolutions derived in (10) and (14) respectively.

B. Impact of Plane Approximation on 3-D THz Imaging

The computational cost of 3-D time-domain THz imaging can be significantly reduced by using the proposed 3-D PCD

method based on the $P \times P$ plane approximation of the range surface. In the second simulation experiment, we investigate how the number P affects the performance of the proposed 3-D PCD THz imaging. Similarly, a point target located at $(0,0,0.48)$ is assumed and the size of the synthetic aperture is set as $3W(z',k_c) \times 3W(z',k_c)$. The images in range and lateral directions reconstructed by using the 3-D PCD method with different P values and the direct correlation method are shown in Fig. 6 respectively. The change in P makes little difference in range imaging since the range compression is directly achieved by IFFT operation before 2-D recursive imaging process. By contrast, the lateral imaging is impacted by P due to the plane approximation in PCD method. As seen in Fig. 6b, a higher peak sidelobe ratio (PSLR) and a
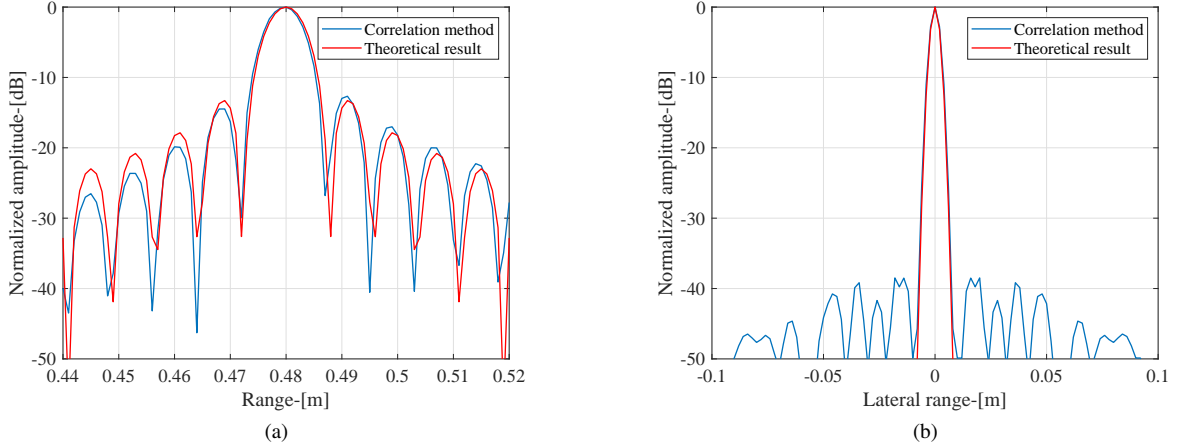
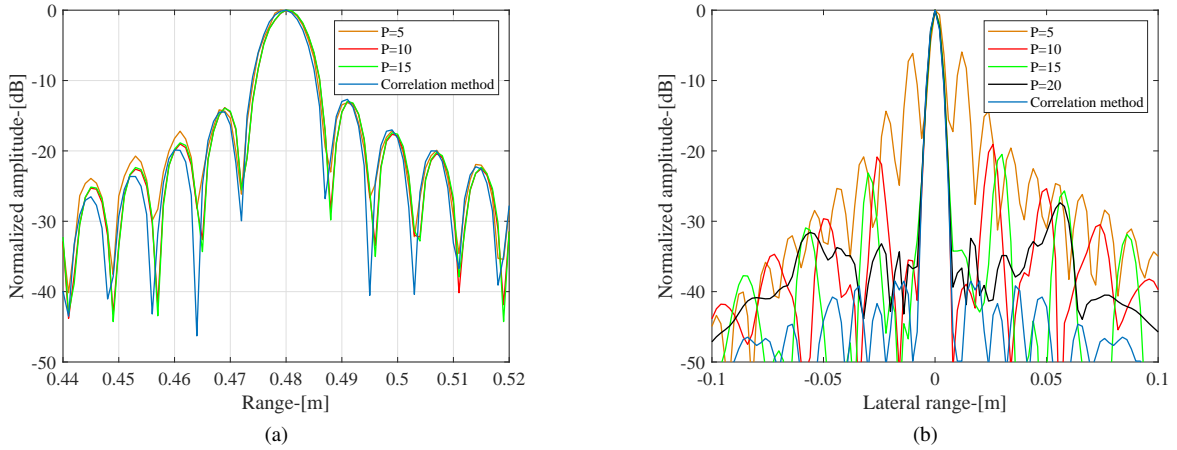Fig. 5. 3-D time-domain correlation THz images in (a) range and (b) lateral directions respectively.

Fig. 6. 3-D PCD THz images with different P in (a) range and (b) lateral directions respectively.
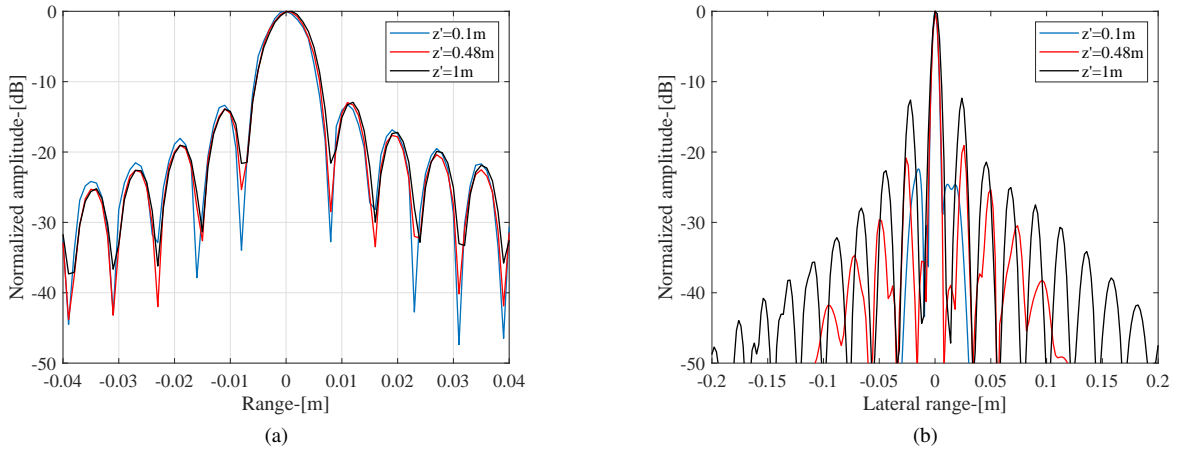

Fig. 7. 3-D PCD THz images with $P = 10$ and different z' in (a) range and (b) lateral directions respectively.

higher integrated sidelobe ratio (ISLR) in lateral image can be achieved with increased P and bounded by that of the time-correlation imaging method shown in Table I, since smaller

planes approximate the range surface more accurately.

With increased range imaging distance, the size of 2-D synthetic aperture becomes larger due to a wider THz beam
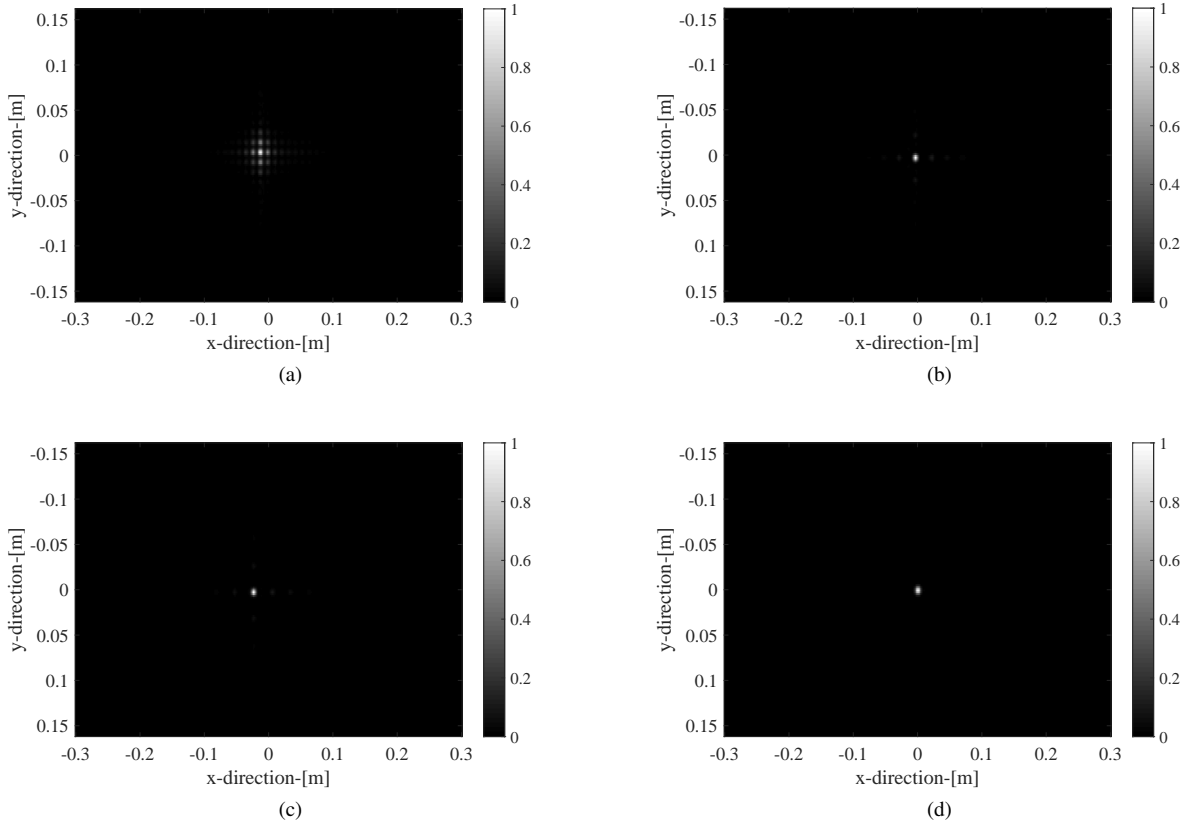
Fig. 8. Given $z' = 0.48$m, ideal 2-D point-target images $I(x', y', 0.48)$ reconstructed by PCD method with $P = 5, 10, 15$ and correlation method are shown in (a), (b), (c) and (d) respectively.

Fig. 9. Optical image of a metal knife.

TABLE I
PSLR AND ISLR COMPARISON

Imaging method	PSLR	ISLR
PCD imaging with P=5	$-5.94dB$	$-1.06dB$
PCD imaging with P=10	$-19.08dB$	$-9.08dB$
PCD imaging with P=15	$-20.49dB$	$-9.54dB$
PCD imaging with P=20	$-27.36dB$	$-10.33dB$
Time-domain correlation	$-38.51dB$	$-10.87dB$

-9.12dB, -9.08dB, -3.64dB respectively when $z' = 0.1$m, 0.48m, and 1m. Therefore, a larger P is required to reconstruct a high-quality image in a long-range PCD imaging.

There is a trade-off between the imaging performance and the computational cost as a larger P makes the PCD implementation more complicated in digital domain. Therefore, a proper selection of P should satisfy a practical imaging requirement. Given $z' = 0.48$m, ideal 2-D point-target images $I(x', y', 0.48)$ reconstructed by PCD method with $P = 5, 10, 15$ and by correlation method are presented in Fig. 8. It is obvious that the ambiguities caused by the plane approximation becomes increasingly negligible when P is larger than 10. In conventional 2-D PCD imaging analysis, an image quality factor related to P derived from the PCD error function can quantify the PCD imaging performance [20]. Given the required image quality, the P can be easily selected. Based on the Gaussian beam model, the slant range variation in lateral direction can be seen as a parabolic function

footprint, thus leading to a worse imaging performance with the same $P \times P$ plane approximation. With $P = 10$, the 3-D PCD images at $z' = 0.1$m, 0.48m, and 1m are reconstructed in range and lateral directions respectively in Fig. 7a and 7b. Similar to Fig. 6a, the plane approximation does not affect the range imaging due to the independent range compression, but the PSLR and ISLR in lateral image becomes lower with a longer range z' due to larger approximation error, where PSLR$= -22.61$dB, -19.08dB, -12.35dB, and ISLR=
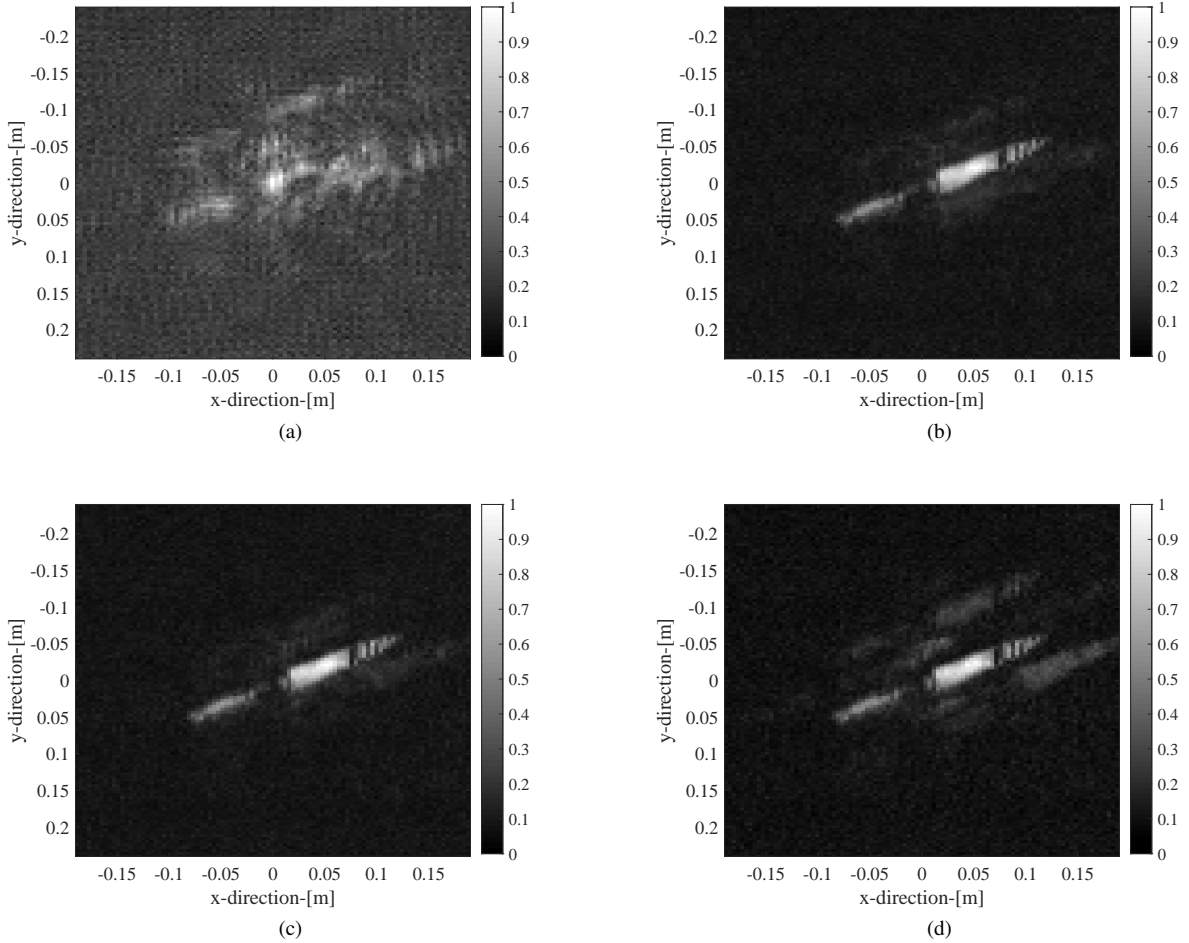
Fig. 10. Reconsturcted 3-D effect images of a metal knife: (a) PCD THz image with $P = 5$, (b) PCD THz image with $P = 10$, (c) PCD THz image with $P = 15$, and (d) time-domain correlation THz image.

similar to the approximation in the 2-D PCD imaging analysis. Therefore, the selection of P in the proposed 3-D PCD imaging can follow the same guideline [20].

C. Complexity Analysis

In the final simulation experiment, we compare the computational cost between the proposed PCD THz imaging method and the time domain correlation method. Due to the same imaging process in range direction, the same 2-D image $I(x', y', 0.48)$ with a size of $0.3m \times 0.6m = 150\Delta y \times 300\Delta x$ is reconstructed by PCD and correlation method respectively with the same parameters adopted in the reconstruction of Fig. 8. Given $z' = 0.48$m, the synthetic aperture size $3W(z', k_c)$ is approximately equal to 0.07m$= 70\Delta y = 70\Delta x$. The number of complex multiplications used to reconstruct an image pixel and the full 2-D image is $71^2 = 5041$ and $151 * 301 * 71^2 \approx 2.3 \times 10^8$ respectively. Based on the 2-D recursive imaging process, the number of complex multiplications can be reduced to $151 * 301 * (3 * 10^2 + 3 * 10 + 1) \approx 1.5 \times 10^7$, thus validating the reduced complexity in the proposed imaging method.

V. EXPERIMENTAL 3-D THZ IMAGING RESULTS

In this section, the real 3-D THz imaging data acquired from the THz imaging system described in Section II are used to validate the proposed 3-D PCD THz imaging method. As seen in Fig. 1, two Ku-band SFCW signals are firstly generated respectively with the same 1.6-GHz bandwidth and a fixed 25-MHz frequency difference. After a $\times 12$ multiplier, the measured THz SFCW signal with a 199.5-GHz center frequency and 19.2-GHz bandwidth is transmitted from the THz antenna. The equivalent beam waist is set to 0.0047 m. With a 0.48-m distance from the observed scene, the THz platform moves along the track described in Fig. 1 and the echoes are received repeatedly with spatial intervals $\Delta x = 0.004$m and $\Delta y = 0.004$m respectively. After another $\times 12$ multiplier, the reference THz SFCW signal with 199.8-GHz center frequency and 19.2-GHz bandwidth is mixed with the scattered echoes and transmitted signal respectively, and then the 300-MHz intermediate frequency (IF) signals are obtained by detectors after the filters. Finally, the baseband complex 3-D THz imaging data can be recovered from the measured and reference signals in digital domain after analog-to-digital converters. The proposed 3-D PCD THz imaging
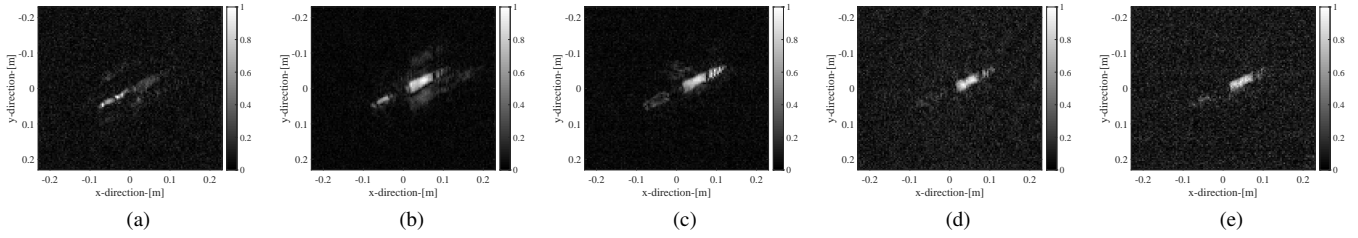
Fig. 11. 3-D slice PCD THz images in lateral direction reconstructed with different ranges $z' = 0.464$m, 0.472m, 0.48m, 0.488m and 0.496m respectively: (a) $I(x', y', 0.464)$, (b) $I(x', y', 0.472)$ (c) $I(x', y', 0.48)$ (d) $I(x', y', 0.488)$ and (e) $I(x', y', 0.496)$.

Fig. 12. 3-D slice time-domain correlation THz images in lateral directions reconstructed with different ranges $z' = 0.464$m, 0.472m, 0.48m, 0.488m and 0.496m respectively: (a) $I(x', y', 0.464)$, (b) $I(x', y', 0.472)$ (c) $I(x', y', 0.48)$ (d) $I(x', y', 0.488)$ and (e) $I(x', y', 0.496)$.
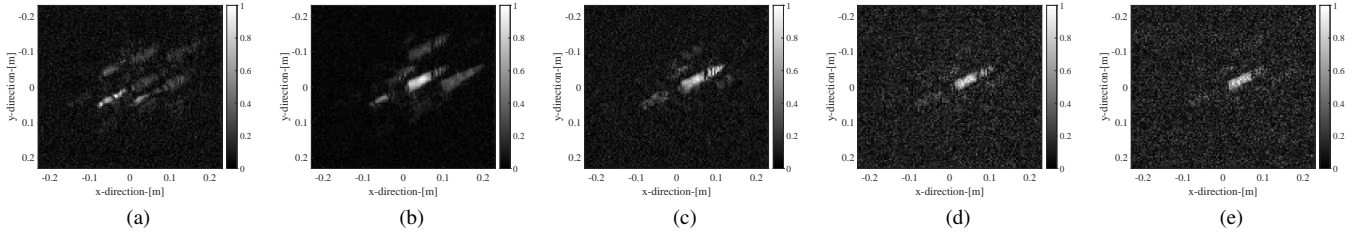
method is finally applied to reconstruct the THz image by using MATLAB2019.

The optical and the reconstructed 3-D effect images of a metal knife are shown in Fig. 9 and Fig. 10 respectively. It is evident that the shape of the knife can be reconstructed accurately by PCD imaging with $P = 10$ and 15 compared with the optical image, thus validating the proposed PCD implementation in a practical THz imaging system. The comparison among Figs. 10a, 10b and 10c shows that a higher quality PCD imaging can be achieved by the increasing P but the improvement is not significant after P is larger than 10. Therefore, $P = 10$ is suitable for this practical system. To simplify and accelerate the THz scanning process in the experiment, the spatial sampling intervals are set to $\Delta x = 4$mm and $\Delta y = 4$mm, thus leading to some tiny ghost targets in Fig. 10. Due to the higher imaging accuracy, these ghost targets are reconstructed more clearly by time-domain correlation method as seen in Fig. 10c and Fig. 10d. Therefore, this experimental results can validate the effectiveness of the time-domain correlation and the proposed PCD imaging methods.

To further demonstrate the 3-D imaging performance in range direction, the 3-D slice images in lateral directions at different ranges from $z' = 0.464$m to $z' = 0.496$m reconstructed by PCD and time-domain correlation methods respectively are shown in Figs. 11 and 12. We can see that the PCD imaging performs very well, similar to the time-domain correlation imaging in range direction. Since the knife handle is closer to the THz platform than the knife blade seen from Fig. 9, the shape of the handle is firstly shown in the reconstructed image $I(x', y', 0.464)$ and gradually disappears when z' is larger. By contrast, the shape of blade becomes clearer in the reconstructed image $I(x', y', 0.496)$.

VI. CONCLUSION

A fast 3-D PCD THz imaging system is proposed in this paper. We firstly introduce the 3-D time-domain correlation THz imaging in terms of the system configuration, THz propagation model and the imaging process in details. The range and lateral resolutions are also demonstrated from the derived close-form expression of the PSF. Based on the plane approximation of the range surface, a 2-D recursive imaging process is developed, by which the computational cost of the correlation method can be significantly reduced. The imaging principle, implementation and complexity analysis are presented, and the simulated and experimental results validate the imaging performance of the proposed 3-D PCD algorithm. The work presented in this paper provides a novel fast synthetic aperture 3-D time-domain THz imaging method.

REFERENCES

[1] N. Llombart, K. B. Cooper, R. J. Dengler, T. Bryllert, and P. H. Siegel, "Confocal Ellipsoidal Reflector System for a Mechanically Scanned Active Terahertz Imager," *IEEE Transactions on Antennas and Propagation*, vol. 58, no. 6, pp. 1834–1841, 2010.
[2] R. Appleby and H. B. Wallace, "Standoff Detection of Weapons and Contraband in the 100 GHz to 1 THz Region," *IEEE Transactions on Antennas and Propagation*, vol. 55, no. 11, pp. 2944–2956, 2007.
[3] H. Liu, H. Zhong, N. Karpowicz, Y. Chen, and X. Zhang, "Terahertz Spectroscopy and Imaging for Defense and Security Applications," *Proceedings of the IEEE*, vol. 95, no. 8, pp. 1514–1527, 2007.
[4] D. Zimdars, J. S. White, G. Stuk, A. Chernovsky, G. Fichter, and S. Williamson, "Security and Non-Destructive Evaluation Application of High Speed Time Domain Terahertz Imaging," in *2006 Conference on Lasers and Electro-Optics and 2006 Quantum Electronics and Laser Science Conference*, 2006, pp. 1–2.
[5] S. Schecklman, G. P. Kniffin, and L. M. Zurk, "Terahertz Non-Destructive Evaluation of Textile Ropes and Slings," in *2014 International Symposium on Optomechatronic Technologies*, 2014, pp. 86–90.
[6] P. H. Siegel, "Terahertz Technology in Biology and Medicine," *IEEE Transactions on Microwave Theory and Techniques*, vol. 52, no. 10, pp. 2438–2447, 2004.

[7] Z. D. Taylor, R. S. Singh, D. B. Bennett, P. Tewari, C. P. Kealey, N. Bajwa, M. O. Culjat, A. Stojadinovic, H. Lee, J. Hubschman, E. R. Brown, and W. S. Grundfest, "Thz medical imaging: in vivo hydration sensing," *IEEE Transactions on Terahertz Science and Technology*, vol. 1, no. 1, pp. 201–219, 2011.

[8] S. S. Ahmed, A. Schiessl, F. Gumbmann, M. Tiebout, S. Methfessel, and L. Schmidt, "Advanced Microwave Imaging," *IEEE Microwave Magazine*, vol. 13, no. 6, pp. 26–43, 2012.

[9] D. M. Sheen, D. L. McMakin, and T. E. Hall, "Three-Dimensional Millimeter-Wave Imaging for Concealed Weapon Detection," *IEEE Transactions on Microwave Theory and Techniques*, vol. 49, no. 9, pp. 1581–1592, 2001.

[10] S. Gu, C. Li, X. Gao, Z. Sun, and G. Fang, "Three-Dimensional Image Reconstruction of Targets Under the Illumination of Terahertz Gaussian Beam—Theory and Experiment," *IEEE Transactions on Geoscience and Remote Sensing*, vol. 51, no. 4, pp. 2241–2249, 2013.

[11] Z. Sun, C. Li, S. Gu, and G. Fang, "Fast Three-Dimensional Image Reconstruction of Targets Under the Illumination of Terahertz Gaussian Beams with Enhanced Phase-Shift Migration to Improve Computation Efficiency," *IEEE Transactions on Terahertz Science and Technology*, vol. 4, no. 4, pp. 479–489, 2014.

[12] W. Liu, C. Li, Z. Sun, Q. Zhang, and G. Fang, "A Fast Three-Dimensional Image Reconstruction With Large Depth of Focus Under the Illumination of Terahertz Gaussian Beams by Using Wavenumber Scaling Algorithm," *IEEE Transactions on Terahertz Science and Technology*, vol. 5, no. 6, pp. 967–977, 2015.

[13] F. Friederich, W. von Spiegel, M. Bauer, F. Meng, M. D. Thomson, S. Boppel, A. Lisauskas, B. Hils, V. Krozer, A. Keil, T. Loffler, R. Henneberger, A. K. Huhn, G. Spickermann, P. H. Bolivar, and H. G. Roskos, "THz Active Imaging Systems With Real-Time Capabilities," *IEEE Transactions on Terahertz Science and Technology*, vol. 1, no. 1, pp. 183–200, 2011.

[14] G. R. Huguenin, "Millimeter wave focal plane array imager," *Proceedings of Spie the International Society for Optical Engineering*, 1994.

[15] Z. Li, J. Wang, J. Wu, and Q. H. Liu, "A Fast Radial Scanned Near-Field 3-D SAR Imaging System and the Reconstruction Method," *IEEE Transactions on Geoscience and Remote Sensing*, vol. 53, no. 3, pp. 1355–1363, 2015.

[16] J. Gao, Y. Qin, B. Deng, H. Wang, and X. Li, "A Novel Method for 3-D Millimeter-Wave Holographic Reconstruction Based on Frequency Interferometry Techniques," *IEEE Transactions on Microwave Theory and Techniques*, vol. 66, no. 3, pp. 1579–1596, 2018.

[17] I. G. Cumming and F. H. Wong, *Digital Processing of Synthetic Aperture Radar Data*, 2005, vol. 1, no. 2.

[18] G. Wang, F. Qi, Z. Liu, C. Liu, C. Xing, and W. Ning, "Comparison Between Back Projection Algorithm and Range Migration Algorithm in Terahertz Imaging," *IEEE Access*, vol. 8, pp. 18 772–18 777, 2020.

[19] D. Liang, M. Wei, J. Gu, Z. Tian, C. Ouyang, J. Han, and W. Zhang, "Broadband Time-Domain Terahertz Radar: Cross Section Measurement and Imaging," in *2015 40th International Conference on Infrared, Millimeter, and Terahertz waves (IRMMW-THz)*, 2015, pp. 1–2.

[20] Y. Nan, X. Huang, and Y. J. Guo, "Piecewise Constant Doppler Algorithm: Performance Analysis, Further Simplification and Motion Compensation," *IEEE Transactions on Aerospace and Electronic Systems*, pp. 1–1, 2020.

[21] ——, "A Millimeter-Wave GCW-SAR Based on Deramp-on-Receive and Piecewise Constant Doppler Imaging," *IEEE Transactions on Geoscience and Remote Sensing*, vol. 58, no. 1, pp. 680–690, 2020.

[22] ——, "Generalized Continuous Wave Synthetic Aperture Radar for High Resolution and Wide Swath Remote Sensing," *IEEE Transactions on Geoscience and Remote Sensing*, vol. 56, no. 12, pp. 7217–7229, 2018.

[23] Goldsmith and P.F., "Quasi-Optical Techniques," *Proceedings of the IEEE*, vol. 80, no. 11, pp. 1729–1747, 1992.